ADVANCED FUNCTIONAL MATERIALS
www.afm-journal.de

Check for updates

Charge Transportation and Chirality in Liquid Crystalline Helical Network Phases of Achiral BTBT-Derived Polycatenar Molecules

Ohjin Kwon, Xiaoqian Cai, Wentao Qu, Feng Liu, Jadwiga Szydłowska, Ewa Gorecka,* Moon Jong Han, Dong Ki Yoon,* Silvio Poppe, and Carsten Tschierske**

First examples of multichain (polycatenar) compounds, based on the π-conjugated [1]benzothieno[3,2-*b*]benzothiophene unit are designed, synthesized, and their soft self-assembly and charge carrier mobility are investigated. These compounds, terminated by the new fan-shaped 2-brominated 3,4,5-trialkoxybenzoate moiety, form bicontinuous cubic liquid crystalline (LC) phases with helical network structure over extremely wide temperature ranges (>200 K), including ambient temperature. Compounds with short chains show an achiral cubic phase with the double network, which upon increasing the chain length, is at first replaced by a tetragonal 3D phase and then by a mirror symmetry is broken triple network cubic phase. In the networks, the capability of bypassing defects provides enhanced charge carrier mobility compared to imperfectly aligned columnar phases, and the charge transportation is non-dispersive, as only rarely observed for LC materials. At the transition to a semicrystalline helical network phase, the conductivity is further enhanced by almost one order of magnitude. In addition, a mirror symmetry broken isotropic liquid phase is formed beside the 3D phases, which upon chain elongation is removed and replaced by a hexagonal columnar LC phase.

1. Introduction

Soft self-assembly of small molecules into stimuli-responsive soft matter structures provides an important route to materials with new functionalities. Liquid crystals (LCs), for example, are important for numerous applications, the best investigated, and the most common being in display technology.[1] But also for steerable antennas in satellite and 5G communication system,[2] as responsive materials for biosensor applications,[3] as active matter,[3] and for photonic applications[4] the LCs are of great importance.[5] In the recent decades, special interest arose in their use as charge carrier materials with adjustable and switchable conduction pathways for ions, electrons, and holes.[6,7] Bicontinuous cubic (Cub_{bi}) LC phases, representing nanosegregated network structures, can form continuous conduction channels in all three spatial directions, thus minimizing distortions induced by structural defects, as demonstrated for ion carrying ionic amphiphiles.[6] For electron/hole carriers, the conduction pathways in all three spatial dimensions are expected to provide an additional entropic advantage for charge separation.[8] However, electron/hole carrier systems require extended (rod-like or disc-like) π-conjugated molecules for which the organization in lamellar or columnar geometries can be more easily achieved[5,9,10,14] than the formation of Cub_{bi} phases with 3D curved structures. Therefore, self-assembled network structures, namely, the double gyroid, were only in rare cases considered,[15,16] usually for polymer systems,[17] forming one or two orders of magnitude larger structures than

O. Kwon, Dr. S. Poppe, Prof. C. Tschierske
Institute of Chemistry
Martin Luther University Halle-Wittenberg
06120 Halle, Germany
E-mail: carsten.tschierske@chemie.uni-halle.de

X. Cai, W. Qu, Prof. F. Liu
State Key Laboratory for Mechanical Behaviour of Materials
Shaanxi International Research Center for Soft Matter
Xi'an Jiaotong University
Xi'an 710049, P. R. China
E-mail: feng.liu@xjtu.edu.cn

The ORCID identification number(s) for the author(s) of this article can be found under https://doi.org/10.1002/adfm.202102271.

© 2021 The Authors. Advanced Functional Materials published by Wiley-VCH GmbH. This is an open access article under the terms of the Creative Commons Attribution-NonCommercial License, which permits use, distribution and reproduction in any medium, provided the original work is properly cited and is not used for commercial purposes.

DOI: 10.1002/adfm.202102271

Dr. J. Szydłowska, Prof. E. Gorecka
Faculty of Chemistry
University of Warsaw
ul. Żwirkii Wigury 101, Warsaw 02-089, Poland
E-mail: gorecka@chem.uw.edu.pl

M. J. Han, Prof. D. K. Yoon
Graduate School of Nanoscience and Technology
Korea Advanced Institute of Science and Technology
Daejeon 34141, Republic of Korea
E-mail: nandk@kaist.ac.kr

Prof. D. K. Yoon
Department of Chemistry and KINC
Korea Advanced Institute of Science and Technology
Daejeon 34141, Republic of Korea

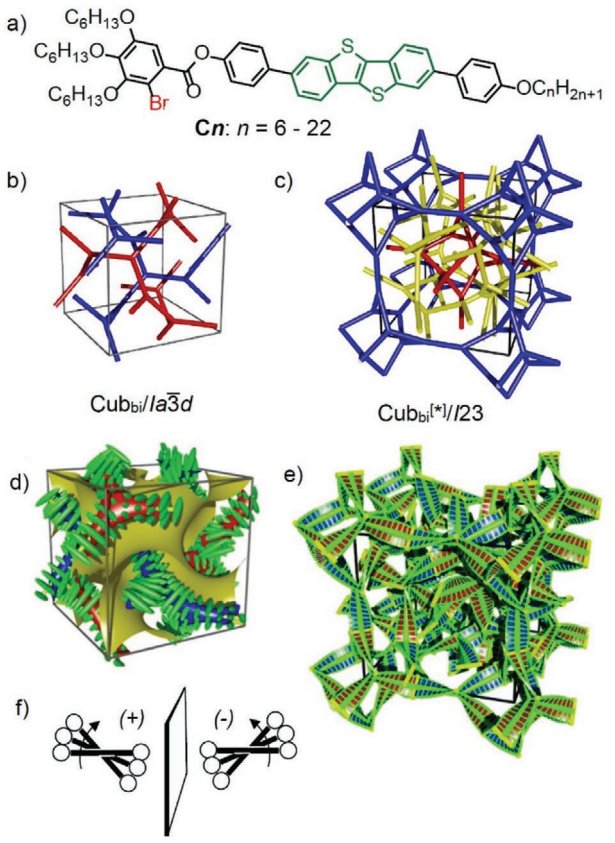

Figure 1. a) Structure of compounds **C*n***, and model showing b,c) the networks and d,e) the helical twist of molecules along the helical networks in the b,d) $Cub_{bi}/Ia\bar{3}d$ phase and the c,e) $Cub_{bi}/I23$ phase; d) the saddle-splay minimal surface between the networks is shown in yellow; f) the helical twist Φ of the molecules developing along the networks; in fact about 3–4 molecules are arranged side-by-side in the lateral cross sections of the network segments, forming rafts which are packed face-to-face along the networks, for clarity only one molecule of adjacent rafts is shown. b–e) Reproduced with permission.[24] Copyright 2020, The Royal Society of Chemistry.

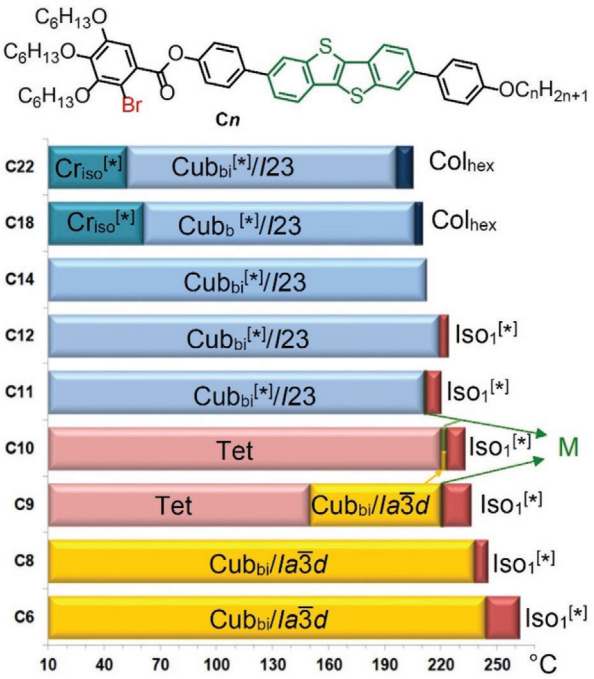

Figure 2. LC phases and phase transitions of compounds **C*n*** as observed on cooling (DSC, rate 10 K min^{-1}); abbreviations: $Cr_{Iso}^{[*]}$ = optically isotropic crystalline mesophase with chiral conglomerate texture; $Cub_{bi}/Ia\bar{3}d$ = bicontinuous cubic phase with double gyroid structure; $Cub_{bi}^{[*]}/I23$ = mirror symmetry broken tricontinuous cubic phase with *I*23 space group; Tet = tetragonal phase, Col_{hex} = hexagonal columnar LC phase; $Iso_1^{[*]}$ = mirror symmetry broken isotropic liquid; and M = metastable highly birefringent 3D mesophase (for **C10** either $Cub_{bi}/Ia\bar{3}d$ or M is formed depending on the conditions; for data on heating, see Figure S2, Supporting Information, and for numerical data with transition enthalpies, see Table S1, Supporting Information), DSC traces are shown in Figure 3a and Figure S1 (Supporting Information).

LCs. This lack of smaller network structures involving efficient charge carrier units is mainly due to the difficulties associated with the design of extended π-conjugated compounds being capable of forming the required curved saddle-splay interfaces in the Cub_{bi} phases.[5,9,18,19]

We have recently introduced a general concept for the design of Cub_{bi} phases based on non-symmetric tri- and tetracatenar compounds involving a semirigid 5,5′-diphenyl-2,2′-dithiophene core unit and three out-fanning alkyl chains at one end.[20] The chain volume was adjusted to the lamellar-columnar cross-over, leading to curvature in all three spatial directions with formation of Cub_{bi} phases where the aromatic units form the networks and the alkyl chain fill the space between them. Due to the organization of these achiral molecules with their long axes almost perpendicular to the networks the bulky trisubstituted ends distort the (anti)parallel alignment of the rods, as a consequence assuming a helical twist along the networks (**Figure 1**f). The network junctions provide a synchronization of the helix sense in the networks.[21,22] There are two distinct types of Cub_{bi} phases with helical network structure as shown in Figure 1b,c. The double gyroid type $Cub_{bi}/Ia\bar{3}d$ phase is composed of two networks which are enantiomorphic and have opposite helicity (red and blue in Figure 1b,d), and hence, their chirality cancels out and this Cub_{bi} phase is achiral.[23] The second one with *I*23 space group (Figure 1c,e) contains three networks, and therefore the helicity cannot cancel and mirror symmetry breaking with chiral conglomerate formation is observed (Figure 3f).[21,24–26]

The [1]benzothieno[3,2-*b*]benzothiophene (BTBT) unit (green in Figure 1a) is known as a highly stable π-conjugated system with the capability of high charge carrier mobility and remarkable performance in photovoltaic devices[27–30] even in smectic[31–33] and columnar LC states.[34,35] However, the BTBT unit is more rigid than the previously used 2,2′-dithiophenes and the organization of these rigid polycyclic π-conjugated BTBTs into Cub_{bi} phases with 3D-curved interfaces is a challenge and has not yet been achieved.

Herein, we report the very first BTBT derived LC compounds **C*n*** (Figure 1a) with helical network structures and predictable morphology ($Ia\bar{3}d$ vs *I*23). This was achieved by using the 2-brominated 3,4,5-trialkoxybenzoyloxy moiety which is introduced as a new general building block for polycatenar molecules,[36] providing wide Cub_{bi} phase ranges including ambient temperature.[37,38] It is shown that the 3D conduction pathway, bypassing

© 2021 The Authors. Advanced Functional Materials published by Wiley-VCH GmbH

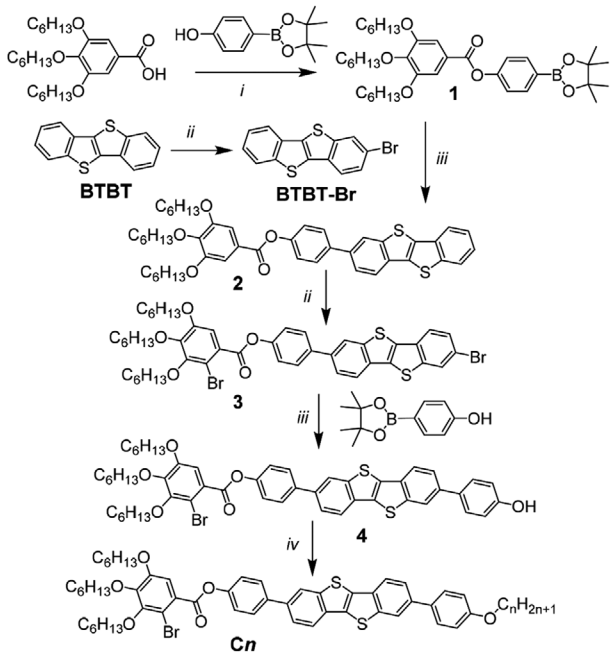

Scheme 1. Synthesis of compounds **C6**–**C22**. Reagents and conditions: i) $SOCl_2$, dry pyridine, RT; ii) Br_2, DCM, RT; iii) THF, sat. $NaHCO_3$ solution, $[Pd(PPh_3)_4]$, reflux; iv) dry 2-butanone, K_2CO_3; TBAI; reflux.

defects, allows nondispersive charge transport which is further enhanced at the transition to a crystalline network phase.

2. Results and Discussions

The compounds C***n*** were synthesized as outlined in **Scheme 1** and described in the Supporting Information. The investigation methods are described in the Experimental Section and the Supporting Information. The mesophases and phase transitions of the series of compounds C***n*** on cooling are shown in **Figure 2**; the transitions on heating are shown in Figure S2 (Supporting Information) and numerical data with associated enthalpy values are collated in Table S1 (Supporting Information). In the following, the soft self-assembly of compounds C***n***, with a focus on their ability of network formation, is described first. Then the charge transportation properties are reported.

2.1. Two Types of Bicontinuous Cubic Network Phases

Depending on the chain length two different Cub_{bi} phases, separated by a tetragonal phase (Tet), can be observed as the dominating mesophases (Figure 2). The small angle X-ray scattering (SAXS) pattern of the Cub_{bi} phase of the short-chain compounds **C6**–**C9** is typical for a cubic lattice with $Ia\bar{3}d$ space group (the double gyroid, Cub_{bi}/ $Ia\bar{3}d$ (**Figure 3**d, Figures S3–S5 and Tables S2–S4 and S6, Supporting Information). For **C6** the lattice parameter is a_{cub} = 10.1 nm at 190 °C (for numerical data, see Table S2, Supporting Information) and about 700 molecules are organized in each unit cell (n_{cell}) with 3–4 molecules are arranged in the cross section of the networks (n_{raft}, see **Table 1**). On cooling

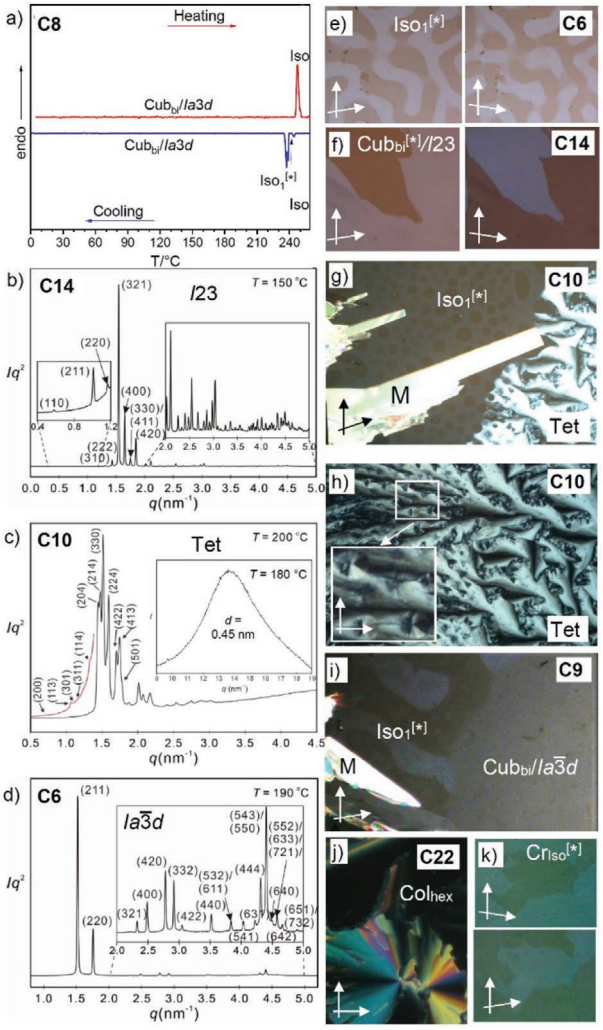

Figure 3. Characterization of the mesophases of compounds C***n***. a) DSC heating and cooling traces (10 K min^{-1}) of **C8**. SAXS patterns of b) **C14**, c) **C10** (the inset shows the diffuse WAXS), and d) **C6** in the distinct phases at the given temperatures with indexation. Representative textures: e) chiral domains of the $Iso_1^{[*]}$ phase of **C6** at 262 °C; f) chiral domains of the $Cub_{bi}^{[*]}$/*I*23 phase of **C14** at 150 °C; g) $Iso_1^{[*]}$-M-Tet transition of **C10** at 220 °C; h) fully developed Tet phase of **C10** at 180 °C; i) $Iso_1^{[*]}$-M-Cub_{bi}/ $Ia\bar{3}d$ transition of **C9** at 221 °C; j) Col_{hex} phase of **C22** at 203 °C; k) conglomerate of the $Cr_{Iso}^{[*]}$ phase of **C22** at 20 °C as observed between slightly uncrossed polarizers (see also Figure S11, Supporting Information).

C6 and **C8** with the shortest chains, the double gyroid phase is retained from 244/238 °C down to 0 °C (Figures 2 and 3a, Figure S1a–c and Table S1, Supporting Information), thus leading to a wide Cub_{bi} phase range of about 240 K. No melting is observed in the second and all following heating scans, meaning that the samples do not crystallize. Only after two years storage at room temperature the sample of **C6** has partly crystallized and a melting of the crystallized parts of the sample of **C6** can be observed at 87 °C (Figure S1a, Supporting Information).

The Cub_{bi}/$Ia\bar{3}d$ phase is observed for compounds **C8**–**C10** with slightly *decreasing* lattice parameter upon chain *elongation* from a_{cub} = 10.1 nm for **C6** to 9.85 nm for **C10** (Table 1). This inverted chain length dependence of a_{cub} is in line with

© 2021 The Authors. Advanced Functional Materials published by Wiley-VCH GmbH

Table 1. Structural data of the mesophases of the investigated compounds.

Compd.	Phase	T [°C]	a,c [nm]	V_{cell} [nm^3]	V_{mol} [nm^3]	n_{cell}	d_{net} [nm]	L_{net} [nm]	n_{raft}	Φ [°]
C6	Cub/$Ia\bar{3}d$	210	10.10	1030	1.284	717	4.37	85.70	3.76	8.87
C8	Cub/ $Ia\bar{3}d$	200	10.00	1000	1.334	670	4.33	84.85	3.55	8.96
C9	Cub/$Ia\bar{3}d$	190	9.98	994	1.358	653	4.32	84.68	3.47	8.98
C9	Tet	180	17.80 20.12	6375	1.358	4191	–	–	–	–
C10	Cub/$Ia\bar{3}d$	230	9.85	956	1.383	617	4.27	83.58	3.32	9.10
C10	Tet	130	17.74 20.32	6395	1.383	4129	–	–	–	–
C11	Tet	170	17.80 20.12	6361	1.408	4034	–	–	–	–
C11	Cub$^{[*]}$/$I23$	200	14.87	3288	1.408	2085	–	307.51	3.05	9.39
C14	Cub$^{[*]}$/$I23$	150	15.20	3512	1.482	2116	–	314.34	3.03	9.19
C22	Cub$^{[*]}$/$I23$	150	16.28	4315	1.681	2292	–	336.67	3.06	8.58
C22	Col$_{hex}$/$p6mm$	205	4.65	8.43	1.681	4.5	–	–	4.5	–

Abbreviations: $V_{cell} = a_{cub}{}^3$ = volume of the unit cell; for the tetragonal phase $V_{cell} = a^2 \times c$, for Col$_{hex}$ phases a height h of 0.45 nm is assumed: $V_{cell} = h(\sqrt{3}a_{hex}{}^2/2)$; V_{mol} = volume of the molecule as calculated with the crystal volume increments of Immirzi;[39] n_{cell} = number of molecules per unit cell, calculated according to 0.893 V_{cell}/V_{mol}, where the factor 0.893 is a correction for the different packing density in the crystalline and the LC state; d_{net} = lateral distance between the nets in the $Ia\bar{3}d$ phase, calculated according to: $d_{net} = \sqrt{3}(a_{cub}/4)$, this value is in good agreement with the molecular length, shown in Figure S9 (Supporting Information) for **C10** and considering the conformational disorder of the alkyl chains; L_{net} = total length of the netwoks per unit cell ($L_{net} = 8.485a_{Ia3d}$ and $L_{net} = 20.68a_{I23}$, respectively);[24] cn_{raft} = number molecules organized in each 0.45 nm tick raft of the networks or columns, calculated according to $n_{raft} = n_{cell}/(L_{net}/0.45)$; for Col$_{hex}$: $n_{raft} = n_{cell}$; Φ = twist angle between adjacent molecules (or rafts of molecules) in the networks of the Cub$_{bi}$ phases; $\Phi(Ia\bar{3}d) = 70.5°/[0.354a_{cub}/0.45\ nm]$, $\Phi(I23) = 90°/[0.290a_{cub}/0.45\ nm]$;[24] for XRD data, see Tables S2–S10 (Supporting Information).

an increasing helical twist Φ with growing chain volume (8.8°–9.1°). As the helical twist between two adjacent junctions of the network is fixed to 70.5° an increasing intermolecular twist reduces the distance between the junctions, thus shrinking the cubic lattice.[20,24] A similar shrinkage of a_{cub} is also observed by rising temperature (for **C8**, as example, from 10.2 nm at 100 °C to 9.9 nm at 240 °C, see Figure S3b, Supporting Information), in this case due to the increasing helical twist caused by thermal alkyl chain expansion. At a certain pitch length, the double gyroid structure becomes instable and is replaced by other LC phases, as follows. For all compounds with n = 11–22 the SAXS pattern of the Cub$_{bi}$ phase can be indexed to the $I23$ space group (Figures S6 and S7a and Tables S7–S9, Supporting Information). The SAXS pattern of compound **C14** is shown as example in Figure 3b. Representative examples of the reconstructed electron density maps of the Cub$_{bi}$/ $Ia\bar{3}d$ phase of **C9** and the Cub$_{bi}$/$I23$ phase of **C22** are shown in **Figure 4**. In accordance with a transition from a double network to a triple network the lattice parameter for the Cub$_{bi}{}^{[*]}$/$I23$ phase is about 50% larger than that in the Cub$_{bi}$/$Ia\bar{3}d$ phase (Table S10, Supporting Information). This Cub$_{bi}$ phase is mirror symmetry broken and forms a conglomerate composed of chiral domains, as identified by investigations between polarizers being rotated by a few (1°–5°) degrees out of the exactly 90° orientation (Figure 3f). Inverting the direction of the rotation inverts the brightness of the domains, thus indicating an optical rotation being in line with the chiral $I23$ lattice.[21,24] In the $Ia\bar{3}d$ phase range the effect of elongation of the relatively short chains is mainly a chain volume effect, increasing the steric distortion at the molecular ends and thus increasing the helical twist Φ (Figure 1f). In contrast, in the $I23$ phases, formed by long chain compounds, chain elongation reduces the helical twist (from 9.4° for **C11** to 8.6° for **C22**, see Table 1). Besides the steric effect, chain elongation simultaneously elongates the molecules, especially if the contribution of *all-trans* segments increases. The elongation of the molecule (at constant chain volume) reduces the twist. For the long-chain compounds **C*n*** the contribution of chain elongation on the molecular length has obviously a stronger twist-reducing effect than the twist-increasing effect provided by the simultaneously growing chain volume.[40]

2.2. Noncubic 3D Phases

At the transition between the two cubic phases two additional birefringent mesophases were observed. For the compounds **C9–C11** a small range of a highly birefringent mesophase (M) with mosaic texture develops on cooling at the transition from the Iso$_1{}^{[*]}$ phase and disappears together with the developing Cub$_{bi}$ phase (Figure 3g,i). However, due to metastability, its investigation was not possible. In addition, a weakly birefringent mesophase with unique texture is observed (Figure 3g,h); for **C9** it appears on cooling below the Cub/$Ia\bar{3}d$ phase at 150 °C and for the next homologue **C10** it replaces the Cub/$Ia\bar{3}d$ phase almost completely. For **C11** it interrupts the Cub$_{bi}{}^{[*]}$/$I23$ phase between 160 and 180 °C upon heating whereas on cooling exclusively the Cub$_{bi}{}^{[*]}$/$I23$ phase is found. The formation of birefringent mesophases with noncubic 3D lattice[41] is obviously associated with the $Ia\bar{3}d$ -$I23$ transition and compound **C10**, located in the middle of this transition forms the broadest region. The SAXS pattern of **C10** can be indexed to a tetragonal lattice with the lattice parameters a_{squ} = 17.74 nm and

© 2021 The Authors. Advanced Functional Materials published by Wiley-VCH GmbH

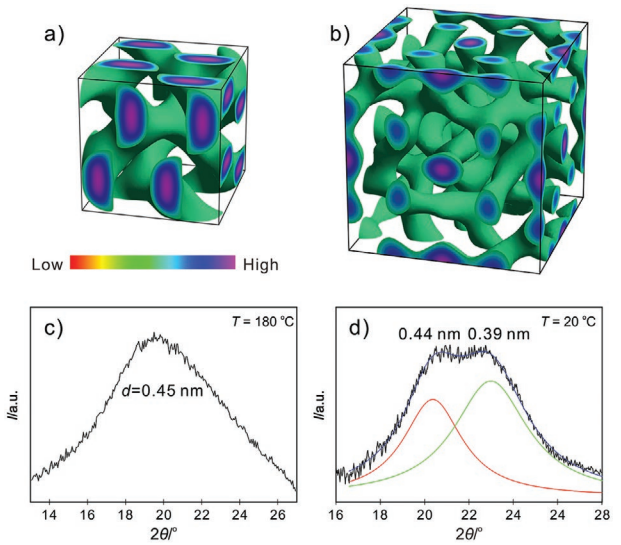

Figure 4. Reconstructed electron density map of the a) Cub_{bi}/ $Ia\bar{3}d$ phase of **C9** and b) $Cub_{bi}^{[*]}$/*I*23 phase of **C22**. The green iso-surfaces enclose the high electron density (blue/purple, aromatic cores) regions of the 3D electron density map. The low electron density (red/yellow) alkyl chain regions are omitted for clarifying the networks (for models, see Figure 1b–e); WAXS diffractogram of the c) $Cub_{bi}^{[*]}$/*I*23 phase of **C14** and d) $Cr_{Iso}^{[*]}$ phase of **C22** with deconvolution into two scattering maxima.

b = 20.32 nm based on the possible highest symmetry space group $P4_2/nnm$ (Figure 3c, for numerical data, see Table S5, Supporting Information). Similar values were found for the related phase of compounds **C9** and **C11** (Table 1). Both lattice parameters are even larger than those of the *I*23 phase and the number of molecules per unit cell (n_{cell}) is approximately doubled from about 2100–2300 in *I*23 to 4050–4650 in Tet (Table 1). As also observed in the adjacent $Ia\bar{3}d$ phase n_{cell} decreases with growing chain length, suggesting that this tetragonal phase is likely to be a helical network phase, too, but assuming a distorted noncubic lattice. Further investigations are required to fully understand these intermediate phases.

2.3. Columnar Phase of C22

For the compounds with the longest chains (n = 18, 22) the Cub_{bi}/*I*23 phase occurs below a small range of a hexagonal columnar (Col_{hex}) phase (for n = 22: a_{hex} = 4.65 nm, see Figure 3j, Figures S7b and S8 and Table S10, Supporting Information). The formation of a columnar phase is in line with the growing interface curvature achieved for compounds with longer chains above a certain temperature. However, the columnar phase is metastable, as it can only be found in the cooling cycles, whereas on heating in all cases a direct Cub_{bi}-Iso transition is observed. It appears that on cooling the chain mobility can be retained at the transition to Col_{hex}, which requires alkyl chain disorder to efficiently fill the space around the columns. In the Cub_{bi} phase, having less mean curvature, a larger reduction of chain disorder is required. This might lead to an entropic penalty for the direct Iso-Cub_{bi} transition on cooling. On the other hand, a larger fraction of *all-trans* chain conformations can be retained in the Cub_{bi} phase which stabilizes the Cub_{bi} phase energetically by denser intermolecular contacts and thus cooperatively inhibits the transition to Col_{hex} on heating. This provides hysteresis and pathway complexity.

2.4. Crystalline Network Phase of C22

In addition, for the two long-chain compounds **C18** and **C22** the transition to an optically isotropic crystalline mesophase with conglomerate texture ($Cr_{Iso}^{[*]}$, see Figure 3k and Figure S11, Supporting Information)[43] is observed on cooling the Cub_{bi}/*I*23 phase, associated with a significant transition enthalpy ($\Delta G \approx$ 30 kJ mol^{-1}, see Figure S1g,h, Supporting Information). The wide-angle X-ray scattering (WAXS) splits into two maxima at d = 0.44 and 0.39 nm (Figure 4d), the latter is attributed to π–π stacking of the crystallized aromatics, whereas the alkyl chains remain in the disordered state; the SAXS becomes diffuse (d = 3.2 nm) which is interpreted as a loss of the cubic lattice, though, chirality synchronization and network structure are retained. Though the $Cr_{Iso}^{[*]}$ phase is metastable with respect to the birefringent crystalline phase (Cr), once formed it is long time stable (>2 years) at ambient temperature. The slow kinetics of the transition $Cr_{Iso}^{[*]}$ to Cr might result from a combination of reduced molecular mobility at lower temperature and the cooperativity, provided by the long-range synchronized helical network structure, providing a significant energetic barrier for the transition to the structurally different birefringent crystalline (Cr) phase.

2.5. Mirror Symmetry Broken Isotropic Liquid Network Phase

Another interesting feature of compounds **C*n*** is the formation of a mirror symmetry broken isotropic liquid ($Iso_1^{[*]}$)[42] between the achiral isotropic liquid (Iso) and the Cub_{bi} phases of compounds **C6–C12** (Figure 2 and Table S1, Supporting Information). For compound **C10** it is a thermodynamically stable (enantiotropic) phase, whereas for the other homologues it is only observed as a monotropic phase on cooling before the Cub_{bi} phase is formed. The $Iso_1^{[*]}$ phase is considered as a percolated liquid formed by a dynamic chirality synchronized helical network without long-range periodic lattice.[42,43] It results from the ordinary isotropic liquid (Iso) by a growing number of network junctions with decreasing temperature. After reaching a critical density of the junctions, chirality synchronization sets in at the Iso-$Iso_1^{[*]}$ transition and mirror symmetry breaking (conglomerate formation, see Figure 3e,i) is observed.[44] Further cooling then leads to the development of a cubic lattice with long-range periodicity, either $Ia\bar{3}d$ with loss of mirror symmetry breaking, or *I*23 by retaining mirror symmetry breaking.

2.6. Charge Carrier Mobility Depending on the Phase Type

The charge carrier mobility of selected compounds was determined by time-of-flight (TOF) measurements as well as in an organic field effect transistor (OFET) device, as described in the Experimental Section.

© 2021 The Authors. Advanced Functional Materials published by Wiley-VCH GmbH

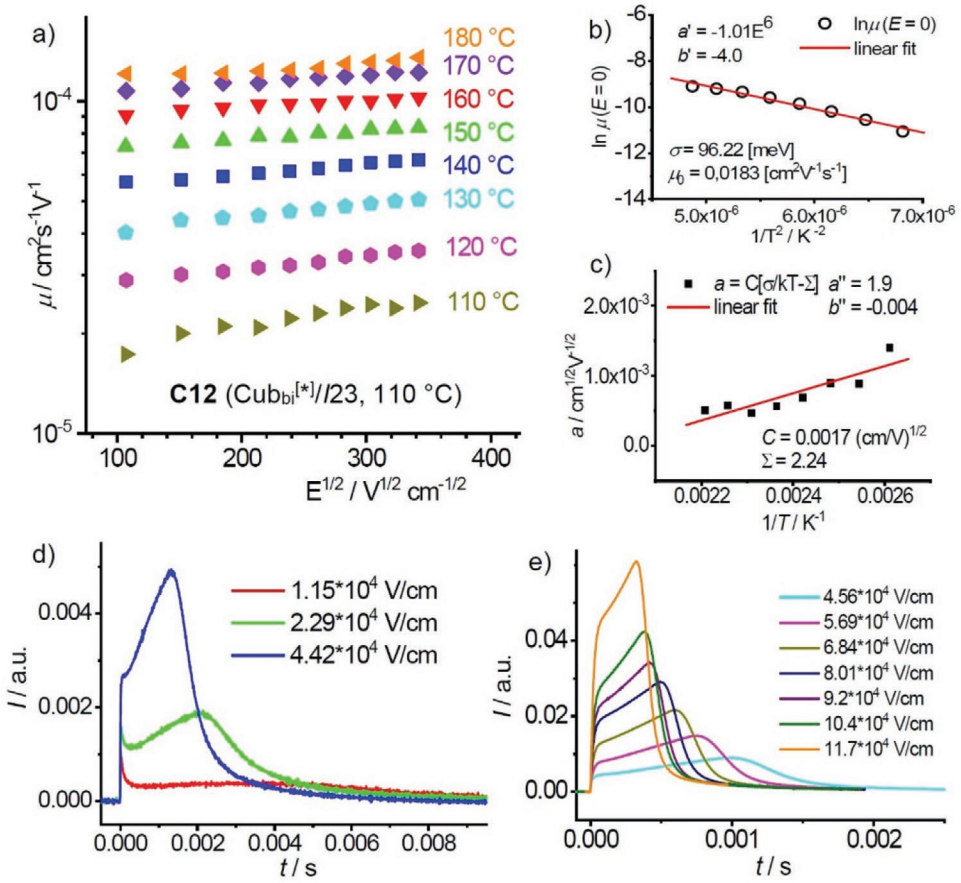

Figure 5. TOF investigation of **C12** in $Cub_{bi}^{[*]}$/I23 phase at 110 °C. a) Field dependence of hole mobility, b) slope *a* of the $\ln\mu(E^{1/2})$ dependence, and c) zero-field hole mobility *b* and $a = C[(\sigma/kT) - \Sigma]$; d,e) TOF transient current of holes at different fields, for details of calculations, see the Experimental Section.

2.6.1. Time-of-Flight Experiments in the I23 Phase of **C12**

The charge carrier mobility in the cubic network phases was measured by TOF experiments for the *I*23 phase of **C12** to be between 1.7×10^{-5} to 1.3×10^{-4} cm^2 V^{-1} s^{-1}, increasing with rising temperature from 110 to 180 °C (**Figure 5**a). Remarkably, the character of hole current versus time is nondispersive with very well-defined cutoff (Figure 5d,e), such features are only rarely observed for LC materials,[45] suggesting a considerably lower number of defects in the structure and lower molecular mobility, than in the other LC phases, thus allowing propagation of the charge wave through the sample without dissipation. Due to the absence of long-range π-stacking interaction between the aromatic cores (indicated by the diffuse wide-angle X-ray scattering with a maximum at 0.45 nm, see Figure 4c as example) and the longer path of the channels transporting the holes/electrons between the electrodes in the complex 3D structure of the Cub_{bi} phases compared to the linear channels in a well-aligned Col_{hex} phase of the same material,[45] the charge carrier mobility is still limited, but it can be significantly enhanced at the transition to a soft crystalline network phase as shown next.

2.6.2. Investigation of OFET Cells of **C22**

The charge carrier mobility of **C22** was measured in modified OFET sandwich cells with bottom-gate bottom-contact (BGBC) configuration (**Figure 6**a), which were prepared as described in the Experimental Section. The OFETs show highly uniform and smooth surface morphology, which improves reproducibility and reliability of the device performance. The electrical properties of the *p*-type **C22**-based OFETs were measured as shown in Figure 6b and Figure S10 (Supporting Information), which allowed the investigation of the relationship between the molecular ordering and charge-carrier (hole) mobility. Figure 6b shows the transfer characteristics of OFETs in the different phases which were simultaneously observed by polarized optical microscopy (POM) (Figure 6c). In the columnar phase at T = 208 °C the sample appears almost isotropic and therefore the dominating alignment of the columns should be perpendicular to the substrate surfaces (Figure 6c, left). Only the small brighter spots indicate some defects due to a not fully perfectly uniform alignment of the columns. With decrease in temperature, the hole mobility increases from 5×10^{-3} cm^2 V^{-1} s^{-1} in Col_{hex} to 8.2×10^{-2} in the Cub_{bi} phase and to 0.56 cm^2 V^{-1} s^{-1} in the $Cr_{Iso}^{[*]}$ phase at lowest temperature (Figure 6b). This shows that the 3D

© 2021 The Authors. Advanced Functional Materials published by Wiley-VCH GmbH

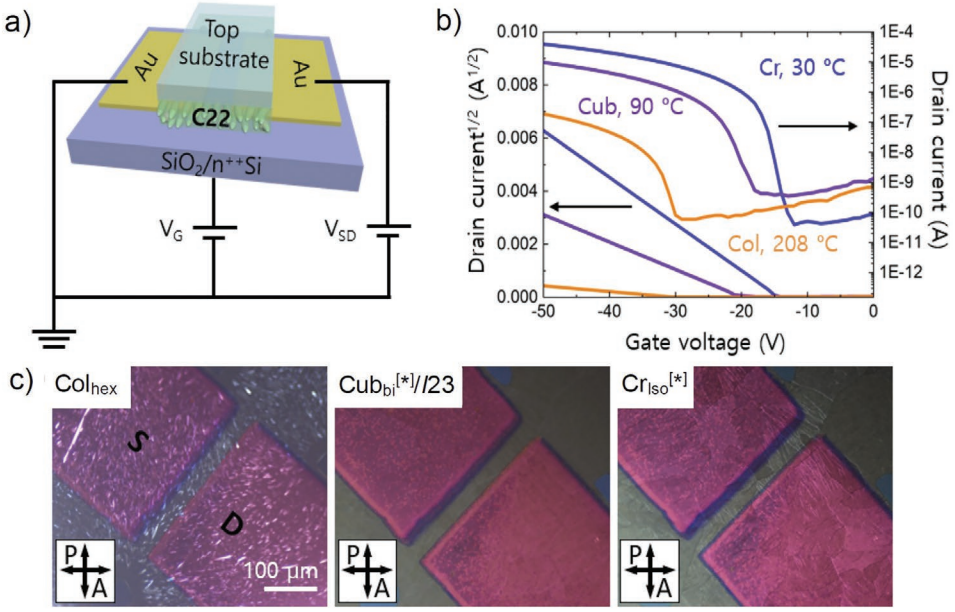

Phase (T/°C)	Mobility ($cm^2V^{-1}s^{-1}$)	I_{ON}/I_{OFF}	V_{th} (V)	Subthreshold Slope (V/dec)
Col_{hex} (208)	$(5 \pm 2.2) \times 10^{-3}$	$\sim 10^3$	$-(32 \pm 8.2)$	~ 9
$Cub_{bi}^{[*]}/I23$ (90)	$(8.2 \pm 2.8) \times 10^{-2}$	$\sim 10^4$	$-(22 \pm 5.3)$	~ 5
$Cr_{Iso}^{[*]}$ (30)	$(5.6 \pm 3.2) \times 10^{-1}$	$\sim 10^5$	$-(15 \pm 3.5)$	~ 4

Figure 6. Electrical properties of **C22**-based organic field effect transistors (OFETs) prepared by sandwich cell. a) Bottom-gate bottom-contact OFETs configuration, b) transfer ($V_{DS} = -50$ V) curves in the different phases, c) POM images and numerical data shown at the bottom, including the average charge carrier mobility, I_{ON}/I_{OFF}, the threshold voltage (V_{th}), and the subthreshold slope (V/dec) which are average values from ten devices.

network structure allows an enhanced charge carrier mobility compared to (imperfectly aligned) columnar phases. Moreover, the charge carrier mobility can be further improved by π-stacking of the crystallized BTBT cores along the networks in $Cr_{Iso}^{[*]}$.

3. Summary and Conclusions

Overall, it is shown that the functional BTBT unit can be incorporated into polycatenar molecules with a tapered 2-bromo-3,4,5-trialkoxybenzoyloxy end and that these compounds can form a wide variety of helical network phases, ranging from soft crystalline via bicontinuous cubic and noncubic 3D phases to mirror symmetry broken liquids. The Cub_{bi} phases cover amazingly wide temperature ranges including ambient temperature and the phase type ($Ia\bar{3}d$ or $I23$) can be controlled by adjusting the intermolecular twist along the networks by chain length modification. As proof of concept, the investigation of OFET cells indicates that the capability of the Cub_{bi} phase for charge transport in all three spatial directions can be advantageous over the 1D transport in the columnar phases and that it can be further enhanced at the transition from LC to crystalline network phases. We expect that further tuning of the molecular structure and blending will improve the charge transport properties in these bicontinuous networks. This provides a new concept for (semi)conducting LCs, complementing the previously known 2D conducting lamellar and 1D conducting columnar systems by the new concept of 3D networks.[15]

In addition, the mirror symmetry broken helical arrays of achiral π-conjugated molecules in the $I23$ phase, initially formed as conglomerate, can assume uniform chirality, either induced by external chirality sources[42] or even spontaneously,[44] and thus can provide uniformly helical soft matter structures and chiral liquids from achiral BTBT derived functional molecules. These spontaneously chiral systems, formed by small molecules and comprising well-organized functional π-conjugated units, provide additional applications going beyond their use as charge carrier materials, for example, as soft and stimuli-responsive materials for photophysical applications like aggregation-induced polarized emission and light harvesting.[4a,46]

4. Experimental Section

Synthesis: The compounds **C*n*** were synthesized as outlined in Scheme 1 and described in detail in the Supporting Information, where also the analytical data are collated. The crude products **C*n*** were purified by column chromatography with (chloroform/*n*-hexane 2/1) and then repeatedly crystallized from THF/EtOH to give colorless solids.

Optical Investigation: Phase transitions were observed by polarizing microscopy (Leica DMR XP) in conjunction with a heating stage (FP 82 HT, Mettler) and controller (FP 90, Mettler). Optical investigation was carried out under equilibrium conditions between glass slides which

© 2021 The Authors. Advanced Functional Materials published by Wiley-VCH GmbH

were used without further treatment, sample thickness was ≈15 µm. Optical microscopy images were taken using a Leica MC120HD camera.

Calorimetric Investigation: Phase transitions were determined by differential scanning calorimetry (DSC-7 and DSC-8000, Perkin Elmer) at heating/cooling rates of 10 K min^{-1} (peak temperatures). If not otherwise noted transition temperatures and enthalpies were taken from the second heating and cooling curve (Figure 3a and Figure S1, Supporting Information).

X-Ray Scattering: In-house X-ray diffraction (XRD) investigations were conducted at Cu Kα line (λ = 1.54 Å) using a standard Coolidge tube source with Ni-filter on powder-like samples. The samples were prepared on a glass plate and were heated to the isotropic state. The powder-like samples were obtained upon fast cooling in the LC phase and were measured in a temperature-controlled heating stage. The distance between sample and the detector was 9 cm (WAXS) or 26.8 cm (SAXS) and the exposure time was 15 min for WAXS and 30 min for SAXS. The diffraction patterns were recorded with a 2D detector (Vantec 500, Bruker), transformation to θ-scan was performed using GADDS.

High-resolution small/wide-angle powder diffraction experiments were recorded on Beamline BL16B1 at Shanghai Synchrotron Radiation Facility (SSRF). Experiments were carried out on solid samples in 1 mm glass capillaries under the control of modified Linkam hot stage with a thermal stability within 0.2 °C. The Pilatus 2M detector was applied in the experiments. q calibration and linearization were testified by using several orders of layer reflections from silver behenate and a series of n-alkanes. The electron density calculation procedure is explained in the Supporting Information.

TOF Measurements: The TOF experiments were performed in a conventional setup, similar to those described in ref. [47]. The 10 µm thick cell was used with ITO electrodes covered with homogeneously aligning surfactant, the cells were filled using capillary forces, the applied voltage was in the range of 11–117 V. All wire connections had grounded screens. The transient photocurrent was measured over 50 kΩ resistor and recorded with 300 MHz digitizing oscilloscope (Agilent Technologies DSO6034A) triggered by the laser pulse. The estimated response time of the whole setup was less than 2.5 µs. The charges (holes and electrons) were generated by a short light pulse (355 nm wavelength, ≈8 ns pulse width) coming from a solid-state laser EKSPLA NL202. The sample was illuminated by a single pulse manually triggered to give the sample enough time for relaxation. To reduce a noise the data were collected over 16 runs and averaged. For the studied material the hole current was stronger, more stable and reproducible than the electron current. The registered hole photocurrent curves were nondispersive, with clear cutoff enabling precise determination the transient time, τ. The transient time τ was determined as the intersection of two lines tangential to the plateau and "current tail." Form the transient time τ the charge (hole) mobility was calculated according to formula: $\mu = d/(\tau E)$, where d is the sample thickness (cm), E is the strength of electric field (V cm^{-1}), and τ is the time of flight (τ/s). The charge mobility generally follows the linear relation, $\log\mu \sim aE^{1/2}$, with the slope a decreasing with increasing temperature.[45b,48] The hole mobility μ was further analyzed assuming 1D charge carrier hopping transport, using the formula with temperature (in K) and field (V cm^{-1}) dependence

$$\mu = \mu_0 \exp\left[-\left(0.9\frac{\sigma}{kT}\right)^2\right]\exp\left\{C\left[\frac{\sigma}{kT}-\sum\right]\sqrt{E}\right\} \quad (1)$$

where prefactor μ_0 is charge mobility at $T\to\infty$, $E = 0$, k is the Boltzmann constant (8.617 × 10^{-3} eV K^{-1}); σ is a standard deviation of Gaussian distribution of energy levels ("diagonal disorder") that are available as hopping sites in holes transport process. The parameter Σ ("off-diagonal disorder") reflects a coupling between transport sites. The parameter μ_0 and σ (standard deviation of energy levels) were obtained by extrapolating the linear dependence $\ln\mu(E^{1/2})$ to $E = 0$ at each temperature and using for $\ln\mu(E = 0)$ the formula

$$b = \ln\mu\,(E=0) = \ln\mu_0 - \left(0.9\sigma/kT\right)^2 \quad (2)$$

with

$$b' = \ln\mu_0;\ a' = -\left(0.9\sigma/k\right)^2 \quad (3)$$

The parameter b as a function of T^{-2} is plotted below and b' and a' parameter of this function are taken from linear fitting. The values of μ_0 and σ parameters are given in Figure 5. Similarly, other coefficients C and Σ describing the charge transport process are calculated from the slopes a of the lines $\ln\mu \approx aE^{1/2}$. Writing $a = C[(\sigma/kT) - \Sigma]$ (formula (1)) and drawing a as a function of T^{-1} the fitted linear parameters are $a'' = C(\sigma/k)$ and $b'' = -C\Sigma$. The found C and Σ are shown in Figure 5.

OFET Cells: The OFETs with a bottom-gate bottom-contact configuration were fabricated on a heavily n-doped silicon wafer as the gate electrode. A 300 nm thick layer of thermally grown SiO_2 served as the gate dielectric layer. The device substrates were cleaned in an ultrasound cleaning bath and sequential rinsing with acetone, ethanol, and deionized water for 15 min each. The 50 nm Au source and drain electrodes with 3 nm Ti as the adhesion layer were both deposited via thermal evaporation using a shadow mask. For a uniform cell gap, the silicon particle with a 1 µm diameter was deposited on the edges of the bottom substrates using UV-curable polymer (NOA 63, Norland Products). The prepared top substrates which are coated with polyimide (PI) were combined with the bottom substrates following UV exposure. The **C22** crystalline powder was prepared on the entrance of the gap, and then heated to around the isotropic phase temperature of **C22** (T_{iso} = 220 °C) to fill the sandwich cell by capillary action.

The transfer characteristics of bottom-gate bottom-contact FETs based on the semiconductor were studied with a Keithley 4200A-SCS semiconductor parameter analyzer. The charge carrier mobility (μ) was calculated by using the following equation from the saturated region in the transfer curve

$$I_{DS} = (WC_i/2L)\mu(V_{GS} - V_{th})^2 \quad (4)$$

where W and L refer to the channel width (500 µm) and length (50 µm), respectively. C_i is the areal capacitance of the SiO_2 gate dielectric (1.04 × 10^{-8} F cm^{-2}), and V_{th} is threshold voltage. V_{th} was extracted via a linear fitting of versus V_G, which is based on the linear transfer data. To avoid mobility attenuation depending on V_G, a sufficient V_G was selected to ensure that the saturation region $V_{GS} \le V_{th}$ and $V_{DS} \le V_{GS} - V_{th}$ is satisfied.[49]

Supporting Information

Supporting Information is available from the Wiley Online Library or from the author.

Acknowledgements

Funding by the European Union (EFRE) is greatly acknowledged. structural characterizations were supported by the National Natural Science Foundation of China (Nos. 21761132033 and 21374086), and OFET investigations were supported by the National Research Foundation (NRF) of Korea funded by the Korean Government (MSIT) (2019K1A3A1A14065772). The authors are grateful to Beamline BL16B1 at SSRF (Shanghai Synchrotron Radiation Facility, China) for providing the beamtime.

Open access funding enabled and organized by Projekt DEAL.

Conflict of Interest

The authors declare no conflict of interest.

Data Availability Statement

The data that support the findings of this study are available in the Supporting Information.

© 2021 The Authors. Advanced Functional Materials published by Wiley-VCH GmbH

Keywords

[1]benzothieno[3, 2-*b*]benzothiophenes, bicontinuous cubic phases, charge transportation, chirality, liquid crystals, mirror symmetry breaking, polycatenar mesogens

Received: March 10, 2021
Published online: May 7, 2021

[1] J. A. Castellano, *The Story of Liquid Crystal Displays and the Creation of an Industry*, World Scientific, Singapore **2005**.
[2] R. Jakoby, A. Gaebler, C. Weickhmann, *Crystals* **2020**, *10*, 514.
[3] E. Bukusoglu, M. B. Pantoja, P. C. Mushenheim, X. Wang, N. L. Abbott, *Annu. Rev. Chem. Biomol. Eng.* **2016**, *7*, 163.
[4] a) Z.-G. Zheng, Y.-Q. Lu, Q. Li, *Adv. Mater.* **2020**, 1905318; b) H. K. Bisoyi, T. J. Bunning, Q. Li, *Adv. Mater.* **2018**, 1706512.
[5] *Handbook of Liquid Crystals*, 2nd ed. (Eds: J. W. Goodby, P. J. Collings, T. Kato, C. Tschierske, H. F. Gleeson, P. Raynes), Wiley-VCH, Weinheim **2014**.
[6] T. Kato, M. Yoshio, T. Ichikawa, B. Soberats, H. Ohno, M. Funahashi, *Nat. Rev. Mater.* **2017**, *2*, 17001.
[7] R. L. Kerr, S. A. Miller, R. K. Shoemaker, B. J. Elliott, D. L. Gin, *J. Am. Chem. Soc.* **2009**, *131*, 15972.
[8] B. A. Gregg, *Phys. Chem. Lett.* **2011**, *2*, 3013.
[9] S. Kutsumizu, *Isr. J. Chem.* **2012**, *52*, 844.
[10] M. O'Neill, S. M. Kelly, *Adv. Mater.* **2011**, *23*, 566.
[11] S. Sergeyev, W. Pisula, Y. H. Geerts, *Chem. Soc. Rev.* **2007**, *36*, 1902.
[12] W. Pisula, M. Zorn, J. Y. Chang, K. Müllen, R. Zentel, *Macromol. Rapid Commun.* **2009**, *30*, 1179.
[13] A. Seki, M. Funahashi, *Heterocycles* **2016**, *92*, 3.
[14] R. Termine, A. Golemme, *J. Mol. Sci.* **2021**, *22*, 877.
[15] To the best of our knowledge, the only Cub_{bi} material which was investigated with respect to charge carrier mobility is based on a bis(4-alkoxybenzoyl)hydrazine core with relatively short π-conjugation length, see ref. [16].
[16] J.-M. Suisse, H. Mori, H. Monobe, S. Kutsumizu, Y. Shimizu, *Soft Matter* **2011**, *7*, 11086.
[17] a) E. J. Crossland, M. Kaperman, M. Nedelcu, C. Ducati, U. Wiesner, D.-M. Smilgies, G. E. S. Toombes, M. A. Hillmyer, S. Ludwigs, U. Steiner, H. J. Snaith, *Nano Lett.* **2009**, *9*, 2807; b) W. Cho, J. Wu, B. S. Shim, W.-F. Kuan, S. E. Mastroianni, W.-S. Young, C.-C. Kuo, T. H. EppsIII, D. C. Martin, *Phys. Chem. Chem. Phys.* **2015**, *17*, 5115.
[18] H. T. Nguyen, C. Destrade, J. Malthete, *Adv. Mater.* **1997**, *9*, 375.
[19] D. W. Bruce, *Acc. Chem. Res.* **2000**, *33*, 831.
[20] C. Dressel, T. Reppe, S. Poppe, M. Prehm, H. Lu, X. Zeng, G. Ungar, C. Tschierske, *Adv. Funct. Mater.* **2020**, 2004353.
[21] C. Dressel, F. Liu, M. Prehm, X. Zeng, G. Ungar, C. Tschierske, *Angew. Chem., Int. Ed.* **2014**, *53*, 13115.
[22] C. Tschierske, G. Ungar, *ChemPhysChem.* **2016**, *17*, 9.
[23] Y. Cao, M. Alaasar, A. Nallapaneni, M. Salamończyk, P. Marinko, E. Gorecka, C. Tschierske, F. Liu, N. Vaupotič, C. Zhu, *Phys. Rev. Lett.* **2020**, *125*, 027801.
[24] X. Zeng, G. Ungar, *J. Mater. Chem. C* **2020**, *8*, 5389.
[25] This phase was previously assigned to the achiral *Im*3*m* space group, but due to chirality it must have a chiral space group. The advantage of the triple network model with *I*23 symmetry over other proposed structures[26] is that there are exclusively three-way junctions, just like in the adjacent double gyroid phase.
[26] a) X. Zeng, G. Ungar, M. Imperor-Clerc, *Nat. Mater.* **2005**, *4*, 562; b) K. Saito, Y. Yamamura, Y. Miwa, S. Kutsumizu, *Phys. Chem. Chem. Phys.* **2016**, *18*, 3280; c) N. Vaupotic, M. Salamonczyk, J. Matraszek, M. Vogrin, D. Pociecha, E. Gorecka, *Phys. Chem. Chem. Phys.* **2020**, *22*, 12814.
[27] H. Ebata, T. Izawa, E. Miyazaki, K. Takimiya, M. Ikeda, H. Kuwabara, T. Yui, *J. Am. Chem. Soc.* **2007**, *129*, 15732.
[28] A. Y. Amin, A. Khassanov, K. Reuter, T. Meyer-Friedrichsen, M. Halik, *J. Am. Chem. Soc.* **2012**, *134*, 16548.
[29] S. Sanda, T. Nagase, T. Kobayashi, K. Takimiya, Y. Sadamitsu, H. Naito, *Org. Electron.* **2018**, *58*, 306.
[30] M. Alkan, I. Yavuz, *Phys. Chem. Chem. Phys.* **2018**, *20*, 15970.
[31] Y. He, M. Sezen, D. Zhang, A. Li, L. Yan, H. Yu, C. He, O. Goto, Y.-L. Loo, H. Meng, *Adv. Electron. Mater.* **2016**, *2*, 1600179.
[32] C. Ruzie, J. Karpinska, A. Laurent, L. Sanguinet, S. Hunter, T. D. Anthopoulos, V. Lemaur, J. Cornil, A. R. Kennedy, O. Fenwick, P. Samorı, G. Schweicher, B. Chattopadhyay, Y. H. Geerts, *J. Mater. Chem. C* **2016**, *4*, 4863.
[33] H. Iino, J. Hanna, *Polym. J.* **2017**, *49*, 23.
[34] C.-X. Liu, H. Wang, J.-Q. Du, K.-Q. Zhao, P. Hu, B.-Q. Wang, H. Monobe, B. Heinrich, B. Donnio, *J. Mater. Chem. C* **2018**, *6*, 4471.
[35] S. Mery, D. Haristoy, J.-F. Nicoud, D. Guillon, S. Diele, H. Monobe, Y. Shimizu, *J. Mater. Chem.* **2002**, *12*, 37.
[36] In previous work on polycatenars Br was used to replace one or two alkyl chains,[18] whereas here it is used as an additional substituent besides the three alkyl chains.
[37] Bromine substitution at the π-conjugated system were used for adjusting the bandgap, see ref. [38].
[38] a) C. Chun, B. Henry, *J. Mol. Spectrosc.* **1976**, *60*, 150; b) S. Wan, C. Chang, J. Wang, G. Yuan, Q. Wu, M. Zhang, Y. Li, *Sol. RRL* **2019**, *3*, 1800250.
[39] A. Immirzi, B. Perini, *Acta Crystallogr., Sect. A* **1977**, *33*, 216.
[40] Though in other cases a re-entrance of the $Cub_{bi}/Ia\bar{3}d$ phase is observed upon chain elongation beyond the existence region of the *I*23 phase,[20,43] this is not found in this case. It appears that the increased molecular length, expanding the lattice, does not allow the transition to a short pitch $Ia\bar{3}d_{(S)}$ phase and would require even smaller twist angles for the alternative transition back to a long pitch $Ia\bar{3}d_{(L)}$ phase.
[41] a) A.-M. Levelut, M. Clerc, *Liq. Cryst.* **1998**, *24*, 105; b) H. Lu, X. Zeng, G. Ungar, C. Dressel, C. Tschierske, *Angew. Chem., Int. Ed.* **2018**, *57*, 2835; c) J. Matraszek, D. Pociecha, N. Vaupotic, M. Salamonczyk, M. Vogrine, E. Gorecka, *Soft Matter* **2020**, *16*, 3882.
[42] C. Dressel, T. Reppe, M. Prehm, M. Brautzsch, C. Tschierske, *Nat. Chem.* **2014**, *6*, 971.
[43] T. Reppe, S. Poppe, X. Cai, Y. Cao, F. Liu, C. Tschierske, *Chem. Sci.* **2020**, *11*, 5902.
[44] C. Tschierske, C. Dressel, *Symmetry* **2020**, *12*, 1098.
[45] a) H. Iino, J. Hanna, *Appl. Phys. Lett.* **2005**, *87*, 132102; b) M. Kastler, F. Laquai, K. Müllen, G. Wegner, *Appl. Phys. Lett.* **2006**, *89*, 252103.
[46] X. Bai, Y. Sun, Y. Jiang, G. Zhao, J. Jiang, C. Yuan, M. Liu, *Angew. Chem., Int. Ed.* **2021**, *60*, 3745.
[47] P. M. Borsenberg, L. Pautmeier, H. Bässler, *J. Chem. Phys.* **1991**, *95*, 1258.
[48] a) H. Bässler, *Phys. Status Solidi* **1993**, *175*, 15; b) M. Funahashi, A. Sonoda, *Phys. Chem. Chem. Phys.* **2014**, *16*, 7754.
[49] M. J. Han, M. McBride, B. Risteen, G. Zhang, B. V. Khau, E. Reichmanis, D. K. Yoon, *Chem. Mater.* **2020**, *32*, 688.

© 2021 The Authors. Advanced Functional Materials published by Wiley-VCH GmbH